

# Bulk and domain-wall effects in ferroelectric photovoltaics

Hiroki Matsuo,<sup>1</sup> Yuuki Kitanaka,<sup>2</sup> Ryotaro Inoue,<sup>3</sup> Yuji Noguchi,<sup>2,\*</sup> Masaru Miyayama,<sup>1,2</sup>  
Takanori Kiguchi,<sup>4</sup> and Toyohiko J. Konno<sup>4</sup>

<sup>1</sup>*Department of Advanced Interdisciplinary Studies, School of Engineering, The University of Tokyo, Tokyo 113-8656, Japan*

<sup>2</sup>*Department of Applied Chemistry, School of Engineering, The University of Tokyo, Tokyo 113-8656, Japan*

<sup>3</sup>*Division of Physics, Institute of Liberal Education, School of Medicine, Nihon University, Tokyo 173-8610, Japan*

<sup>4</sup>*Institute of Materials Research, Tohoku University, Sendai 980-8577, Japan*

(Received 27 May 2016; revised manuscript received 16 October 2016; published 19 December 2016)

We investigate the photovoltaic (PV) effects in ferroelectrics based on the polar structure in domains and the intrinsic symmetry breaking of ferroelastic domain walls (DWs). A comprehensive analysis for BiFeO<sub>3</sub> films with the single-domain and 71° domain structures reveals a major contribution of the DWs superimposed on the bulk PV effect, which can explain the enhanced PV response in the multidomain film exhibiting photovoltages greater than the band gap. Our methodology can reveal the contributions of the bulk PV and the DW-PV effects quantitatively and uncover a design strategy for enhancing ferroelectric photovoltaics.

DOI: [10.1103/PhysRevB.94.214111](https://doi.org/10.1103/PhysRevB.94.214111)

## I. INTRODUCTION

Ferroic materials, such as ferromagnetics [1], ferroelastics [2], and ferroelectrics [3–5], are of great scientific and technological interest because the spin, strain, and polarization degrees of freedom can be strongly coupled in response to external stimuli [6,7]. The ferroic crystals naturally split into domains separated by domain walls (DWs) [8,9]. Exploiting the function of ferroic DWs often enables control over physical properties beyond those obtained for single crystals in single-domain (SD) states [10,11].

Multiferroic BiFeO<sub>3</sub> (BFO) is known to exhibit ferroelectric and antiferromagnetic orders above room temperature [12,13]. Because of the symmetry and mechanical constraints, rhombohedral BFO crystals generally accommodate ferroelectric and ferroelastic DWs. Provided that a net polarization is directed away from the polar axis, a mesoscopic structure involving 71° or 109° ferroelastic DWs appears [14]. One of the fascinating properties of BFO in a multidomain (MD) state is high photovoltages generated under illumination; these voltage values far exceed the voltage corresponding to the bulk band gap [15,16]. However, there has been considerable debate over the origin of the photovoltaic (PV) effect that generates the anomalously high voltages, owing to a lack of precise information on the bulk PV (BPV) tensor in SD states.

Essentially, the PV effect in ferroelectrics stems from the noncentrosymmetry in their polar crystals [17–19]. High-resolution transmission electron microscopy analysis and first-principles calculations have demonstrated that ferroelastic DWs involve the intrinsic symmetry breaking arising from a spatial rotation of spontaneous polarization ( $\mathbf{P}_s$ ) [20]. A recent study on ferroelectric BaTiO<sub>3</sub> single crystals has shown that the DW-PV effect derived from the distinct polar structure in 90° DW regions is superimposed on the BPV effect [21]. To provide a guideline for ferroelectrics exhibiting a high-efficiency PV response, we need to understand how the BPV and DW-PV effects affect the PV properties.

In this paper, we report an analysis of the PV properties of BFO films with SD and MD structures based on the BPV and DW-PV effects. We show that the DW-PV effect dominates the photoresponse of the BFO film with 71° DWs over the BPV effect. Our methodology provides reliable, unambiguous information about the physical origin of the PV effect of ferroelectrics with ferroelastic DWs.

## II. EXPERIMENTS

Ferroelectric BFO thin films with a thickness of 300 nm were prepared on SrTiO<sub>3</sub> (STO) (100) single-crystal substrates by a pulsed-laser deposition (PLD) method with a KrF excimer laser. For the deposition of the BFO films, a substrate temperature, an oxygen pressure, laser energy, and a laser repetition rate were set at 630 °C, 11 Pa, 1.2 J/cm<sup>2</sup>, and 7 Hz, respectively. To control domain structures, we used two different vicinal substrates with a miscut angle of 4° along the [110] (STO<sub>v-[110]</sub>) and [010] (STO<sub>v-[010]</sub>) directions [22,23]. A SD film was grown on the STO<sub>v-[110]</sub> substrate. To obtain a MD film with an ordered 71° domain structure, we deposited a Ba<sub>0.5</sub>Sr<sub>0.5</sub>TiO<sub>3</sub> (BST) buffer layer with a thickness of 200 nm on the STO<sub>v-[010]</sub> substrate. The BST buffer layer was deposited at 670 °C with an oxygen pressure of 2.7 Pa. The laser energy was 1.2 J/cm<sup>2</sup> and the laser repetition rate was 1 Hz. The domain structure of the films grown on the STO<sub>v-[110]</sub> substrate and the STO<sub>v-[010]</sub> substrate were investigated by piezoresponse force microscopy (PFM), x-ray diffraction (XRD), and annular-bright-field scanning transmission electron microscopy (ABF-STEM) measurements.

The PV properties in various crystallographic directions (where the pseudocubic notation is adopted) were measured under illumination with light at a wavelength of 405 nm ( $h\nu = 3.1$  eV). The power of the incident light was set at 2.5 W/cm<sup>2</sup>. Taking into account the 4° vicinal angle from the pseudocubic axes precisely, we use the lab-coordinate ( $xyz$ ) system [see Fig. 1(e) for the SD sample and (f) for the MD sample] to express the directions of linearly polarized light ( $h\nu$ ), photocurrent density ( $J$ ), and photovoltage ( $V$ ). In the measurement configurations,  $h\nu$  with a polarization angle ( $\omega$ ) from the  $y$  axis in the  $xy$  plane propagates along the  $z$  axis

\*ynoguchi@fmat.t.u-tokyo.ac.jp

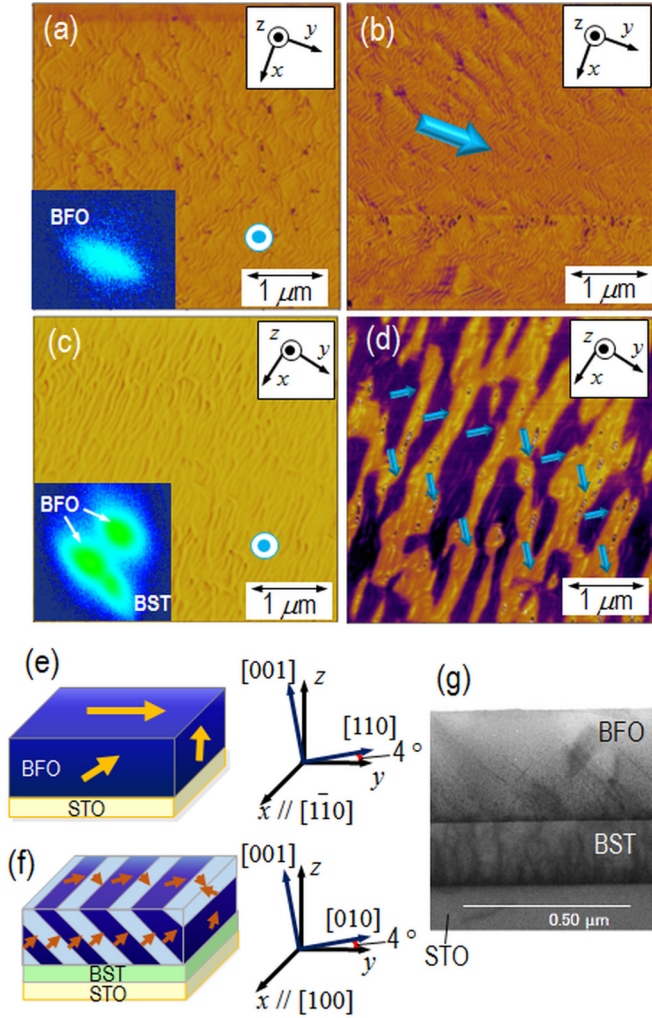


FIG. 1. Domain structures of BFO thin films. Piezoresponse force microscopy (PFM) images: (a) Out-of-plane (OOP) and (b) in-plane (IP) phase images show the single-domain (SD) structure of the film on  $\text{STO}_{v-[110]}$ . (c) OOP and (d) IP phase images display a multidomain (MD) structure with  $71^\circ$  domain walls of the film on  $\text{STO}_{v-[010]}$ . X-ray diffraction reciprocal space maps of 113 reflections are shown in the insets in (a) and (c). Bold, blue arrows depict the IP components of  $\mathbf{P}_s$  and blue circles with a dot indicate the OOP components of  $\mathbf{P}_s$ , where the directions of the lab-coordinate ( $xyz$ ) system are shown. Schematics of the (e) SD ( $\text{STO}_{v-[110]}$ ) and (f) MD ( $\text{STO}_{v-[010]}$ ) structures, with solid arrows indicating the components of  $\mathbf{P}_s$  in each of the domains. The relationships between the pseudocubic and lab-coordinate ( $xyz$ ) axes are also shown. (g) Annular bright-field image of the cross section in the MD ( $\text{STO}_{v-[010]}$ ) sample.

and is incident on the sample surface. For the SD sample, the  $x$  axis lies along  $[1\bar{1}0]$  and the  $y$  and  $z$  axes are  $4^\circ$  away from  $[110]$  and  $[001]$ , respectively [Fig. 1(e)]. In the case of the MD film, the  $x$  axis coincides with  $[100]$  and the  $y$  and  $z$  axes are  $4^\circ$  away from  $[010]$  and  $[001]$ , respectively [Fig. 1(f)]. We denote short-circuit current density ( $J_{sc}$ ) and open-circuit voltage ( $V_{oc}$ ) in the  $m$  direction of the SD film by  $J_{m,SD}$  and  $V_{m,SD}$ , respectively, and define those of the MD film as  $J_{m,MD}$  and  $V_{m,MD}$ , respectively. The positive directions of  $J$  and the bias voltage ( $V_{bias}$ ) are set in the  $m$  direction: positive  $J_m$  indicates

a photocurrent that flows in the  $m$  direction and becomes zero at  $V_{bias} = -V_m$ . We examined the  $\omega$  dependences of  $J_{x,SD}$ ,  $J_{y,SD}$ , and  $J_{y,MD}$  to evaluate the elements of the PV tensor.

### III. RESULTS AND DISCUSSION

Figure 1 shows the out-of-plane (OOP) and in-plane (IP) PFM phase images of the films grown on the  $\text{STO}_{v-[110]}$  and  $\text{STO}_{v-[010]}$  substrates. The film ( $\text{STO}_{v-[110]}$ ) presents uniform contrast in both the OOP [Fig. 1(a)] and the IP [Fig. 1(b)] images, indicating the SD structure with  $\mathbf{P}_s$  along the approximate  $[111]$  direction. Although the film ( $\text{STO}_{v-[010]}$ ) exhibits uniform contrast in the OOP image [Fig. 1(c)], it shows a characteristic MD pattern in the IP image [Fig. 1(d)]. This result shows that two polarization variants exist in the IP direction, constructing a  $71^\circ$  domain structure. The analysis of x-ray diffraction reciprocal space maps (XRD-RSMs) shows that both the films on the  $\text{STO}_{v-[110]}$  and  $\text{STO}_{v-[010]}$  substrates exhibit a monoclinic ( $M_A$ ) structure with  $\mathbf{P}_s$  slightly tilted from the  $[111]$  to the  $[001]$  direction. Because the elongation of the  $(001)$  lattice spacing caused by the monoclinic distortion is less than 0.5% with respect to the bulk BFO in rhombohedral  $R3c$  symmetry, the space group of the BFO films can be regarded as  $R3c$ . In the XRD-RSMs of the 113 reflection [the insets in Figs. 1(a) and 1(c)], a single peak derived from the SD structure was detected for the film ( $\text{STO}_{v-[110]}$ ), whereas a doublet arising from the  $71^\circ$  domain (MD) structure was observed for the film ( $\text{STO}_{v-[010]}$ ). These XRD results are consistent with the PFM observations. An ABF-STEM image of a cross section of the MD film [Fig. 1(g)] reveals that the  $71^\circ$  domain walls have a platelike plane underneath the surface and that the domain width is in the range of 100–400 nm.

In Fig. 2, we display the  $\omega$  dependences of  $J_{y,SD}$ ,  $J_{x,SD}$ , and  $J_{y,MD}$ , along with the measurement configurations. Although

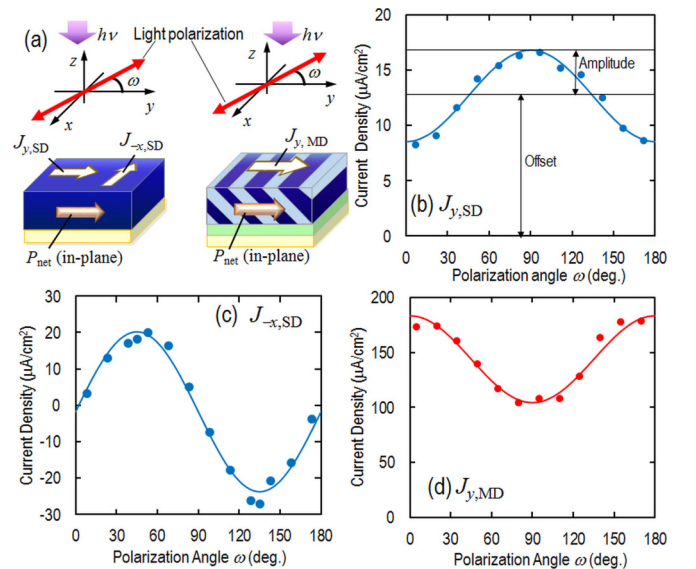


FIG. 2. (a) PV measurement configurations of the SD and MD samples; polarized light ( $h\nu$ ) propagates along the  $z$  axis with a light polarization angle  $\omega$  from the  $y$  axis in the  $xy$  plane. Short-circuit currents (b)  $J_{y,SD}$  and (c)  $J_{x,SD}$  in the SD film and (d)  $J_{y,MD}$  in the MD film as a function of  $\omega$ .

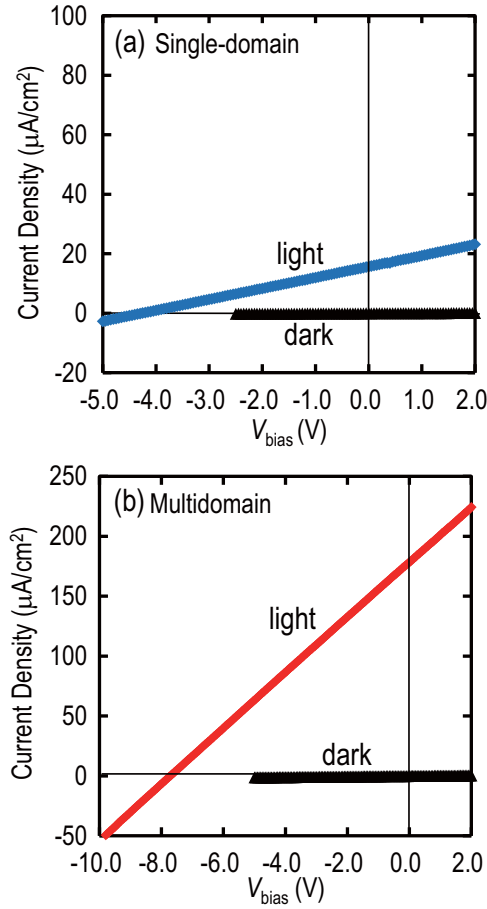


FIG. 3. Current density-bias voltage ( $J$ - $V_{\text{bias}}$ ) properties along the  $y$  direction under dark conditions and under illumination ( $h\nu = 3.1$  eV), as observed for (a) the SD film ( $\omega = 90^\circ$ ) and (b) the MD film ( $\omega = 0^\circ$ ).

the  $J_{-x,\text{SD}}$  [Fig. 2(c)] has a single component of a sinusoidal dependence on  $\omega$ ,  $J_{y,\text{SD}}$  [Fig. 2(b)] and  $J_{y,\text{MD}}$  [Fig. 2(d)] contain apparent offsets of  $J_{y,\text{SD,off}}$  and  $J_{y,\text{MD,off}}$  in addition to their respective sinusoidal oscillations with amplitudes of  $J_{y,\text{SD,amp}}$  and  $J_{y,\text{MD,amp}}$ .

Figure 3 presents the  $J$ - $V_{\text{bias}}$  properties under dark and light illumination observed for the SD film ( $m = y, \omega = 90^\circ$ ) [Fig. 3(a)] and the MD film ( $m = y, \omega = 0^\circ$ ) [Fig. 3(b)]. With these light polarization angles, each  $J_{\text{sc}}$  becomes the maximum value. The MD film shows a high  $V_{y,\text{MD}}$  (7.7 V) compared with that of the SD film ( $V_{y,\text{SD}} = 4.2$  V). Moreover, the  $J_{y,\text{MD}}$  ( $180 \mu\text{A}/\text{cm}^2$ ) is more than ten times larger than the  $J_{y,\text{SD}}$  ( $17 \mu\text{A}/\text{cm}^2$ ).

When ferroelectric crystals are illuminated with linearly polarized light, photocurrent density  $\mathbf{J}$  arising from the BPV effect is expressed by the following equation using a third-rank BPV tensor  $\beta_{ijk}$ :

$$\mathbf{J}_i = I_{\text{opt}} \beta_{ijk} \mathbf{e}_j \mathbf{e}_k, \quad (1)$$

where  $I_{\text{opt}}$  denotes the light intensity and  $\mathbf{e}_j$  and  $\mathbf{e}_k$  are the components of the unit vectors along the  $j$  and  $k$  directions in a crystallographic coordinate system, respectively. We use the Einstein summation convention in Eq. (1). Considering that  $I_{\text{opt}}$  decays inside the BFO films because of

light absorption, we can write  $I_{\text{opt}}$  using film thickness ( $d$ ), incident light intensity ( $I_{\text{incident}}$ ), and absorption coefficient ( $\alpha = 2.1 \times 10^5 \text{ cm}^{-1}$ ) as  $I_{\text{opt}} = I_{\text{incident}} \frac{1 - \exp(-\alpha d)}{\alpha d}$ , where  $I_{\text{opt}}$  denotes thickness-averaged light intensity ( $0.4 \text{ W}/\text{cm}^2$  for our films) [24].

Here, we consider the  $J_{\text{sc}}$  derived from the BPV effect with  $h\nu$  along the [001] direction. For the SD film [Fig. 1(e)], the photocurrents along the [110] and  $[\bar{1}10]$  directions are defined as  $J_{[110]}^{\text{bulk}}$  and  $J_{[\bar{1}10]}^{\text{bulk}}$ , respectively. We can express  $\frac{J_{[110]}^{\text{bulk}}}{I_{\text{opt}}}$  by

$$\frac{J_{[110]}^{\text{bulk}}}{I_{\text{opt}}} = \beta_{[110],\text{off}}^{\text{bulk}} + \beta_{[110],\text{amp}}^{\text{bulk}} \sin \left[ 2 \left( \omega + \frac{\pi}{4} \right) \right], \quad (2)$$

$$\frac{J_{[\bar{1}10]}^{\text{bulk}}}{I_{\text{opt}}} = \beta_{[\bar{1}10],\text{amp}}^{\text{bulk}} \sin 2\omega, \quad (3)$$

where the subscripts “amp” and “off” indicate the amplitude of the sine function and the offset, respectively. The symmetry constraint of  $C_{3v}$  leads to the following relations:  $\beta_{[110],\text{off}}^{\text{bulk}} = \frac{1}{3\sqrt{3}}(\sqrt{2}\beta_{15} + \beta_{22} + 2\sqrt{2}\beta_{31} + \sqrt{2}\beta_{33})$ ,  $\beta_{[110],\text{amp}}^{\text{bulk}} = \frac{1}{3\sqrt{3}}(\sqrt{2}\beta_{15} - 2\beta_{22} - \sqrt{2}\beta_{31} + \sqrt{2}\beta_{33})$ , and  $\beta_{[\bar{1}10],\text{amp}}^{\text{bulk}} = \frac{2}{\sqrt{6}}\beta_{15} + \frac{1}{\sqrt{3}}\beta_{22}$ , where we use matrix notation to express the elements of  $\beta_{ijk}$ .  $J_{[\bar{1}10]}^{\text{bulk}}$  involves only the sine function, whereas the  $J_{[110]}^{\text{bulk}}$  involves the offset and the  $\omega$ -dependent sine function. In our experiments, we measured  $J_{y,\text{SD}}$  and  $J_{-x,\text{SD}}$ , which differ slightly from  $J_{[110]}^{\text{bulk}}$  and  $J_{[\bar{1}10]}^{\text{bulk}}$  because of the  $4^\circ$  vicinal angle. The equations of  $\frac{J_{y,\text{SD}}}{I_{\text{opt}}}$  and  $\frac{J_{-x,\text{SD}}}{I_{\text{opt}}}$  are described in Eqs. (S19) and (S20) in the Supplemental Material [25]. Fitting the  $J_{y,\text{SD}}$  and  $J_{-x,\text{SD}}$  data by using these equations yields the elements of the BPV tensor, as listed in Table I; the experimental data are well described by the fitting curves.

For the MD film,  $J_{\text{sc}}$  along the [010] direction,  $J_{[010],\text{MD}}^{\text{bulk}}$ , is expressed as

$$\frac{J_{[010],\text{MD}}^{\text{bulk}}}{I_{\text{opt}}} = \beta_{[010],\text{MD,off}}^{\text{bulk}} + \beta_{[010],\text{MD,amp}}^{\text{bulk}} \sin \left[ 2 \left( \omega + \frac{3\pi}{4} \right) \right], \quad (4)$$

where  $\beta_{[010],\text{MD,off}}^{\text{bulk}} = \frac{1}{3\sqrt{3}}(\beta_{15} + \frac{1}{\sqrt{2}}\beta_{22} + 2\beta_{31} + \beta_{33})$ , and  $\beta_{[010],\text{MD,amp}}^{\text{bulk}} = -\frac{1}{\sqrt{3}}\beta_{15} - \frac{1}{\sqrt{6}}\beta_{22}$ . Because of the  $4^\circ$  vicinal angle,  $J_{[010],\text{MD}}^{\text{bulk}}$  must be replaced by  $J_{y,\text{MD}}^{\text{bulk}}$  [see Eq. (S30) in the Supplemental Material]. The BPV tensor elements precisely determined for the SD film yields  $J_{y,\text{MD}}^{\text{bulk}} = 24 \mu\text{A}/\text{cm}^2$ , which is considerably smaller than the experimental  $J_{y,\text{MD}}$  ( $180 \mu\text{A}/\text{cm}^2$ ). We note that the PV data observed for the MD film cannot be explained solely by the BPV effect.

Here, we discuss the reason why the PV response in the MD film is not described by the BPV effect. Bhatnagar *et al.* have reported that the conducting behavior at ferroelastic DWs plays a decisive role in the PV properties observed for BFO films and that the high photovoltages can be achieved by controlling the conductivity ( $\sigma$ ) of the DWs [16]. Under illumination, even though our MD film exhibits a higher  $\sigma$  of  $9.1 \times 10^{-7} \text{ S cm}^{-1}$  in the  $y$  direction ( $1.5 \times 10^{-7} \text{ S cm}^{-1}$  for the SD film), the



TABLE I. Photovoltaic elements of the BFO films under  $h\nu = 3.1$  eV.

$\beta_{15}(\text{V}^{-1})$	$\beta_{22}(\text{V}^{-1})^a$	$\beta_{31}(\text{V}^{-1})$	$\beta_{33}(\text{V}^{-1})$	$\beta_{\text{off}}^{\text{DW}}(\text{V}^{-1})$	$\beta_{\text{amp}}^{\text{DW}}(\text{V}^{-1})$
$8.2 \times 10^{-5}$	$-1.1 \times 10^{-5}$	$6.4 \times 10^{-5}$	$-1.1 \times 10^{-4}$	$3.5 \times 10^{-4}$	$-5.7 \times 10^{-5}$

<sup>a</sup>The relation of  $\beta_{22} = \frac{\beta_{33}}{10}$  is used for the analysis [24,26].

MD film indeed shows a higher photovoltage (see Fig. 3). This experimental observation demonstrates that the conductivities of the DWs do not dominate the overall behavior and suggests that the  $71^\circ$  DWs themselves contribute substantially to the PV response in the MD film.

We consider that the experimental data of the MD film arise from not only the BPV effect but also the DW-PV effect. Here, we assume that the DW-PV effect has an offset  $\beta_{\text{off}}^{\text{DW}}$  and a sine function with an amplitude  $\beta_{\text{amp}}^{\text{DW}}$ . Taking into account the BPV and DW-PV effects, we can describe  $\frac{J_{[010],\text{MD}}}{I_{\text{opt}}}$  by

$$\frac{J_{[010],\text{MD}}}{I_{\text{opt}}} = (\beta_{\text{off}}^{\text{DW}} + \beta_{[010],\text{MD},\text{off}}^{\text{bulk}}) + (\beta_{\text{amp}}^{\text{DW}} + \beta_{[010],\text{MD},\text{amp}}^{\text{bulk}}) \times \sin \left[ 2 \left( \omega + \frac{3}{4} \pi \right) \right]. \quad (5)$$

In a similar manner to the SD film, we must replace  $J_{[010],\text{MD}}$  by  $J_{y,\text{MD}}$  [see Eq. (S31) in the Supplemental Material]. The experimental data can be well fitted by this equation, leading to the values of  $\beta_{\text{off}}^{\text{DW}}$  and  $\beta_{\text{amp}}^{\text{DW}}$  listed in Table I.

To compare the BPV and DW-PV effects, we first derive the maximum PV coefficient in the SD state by taking into account the crystal orientation dependence of the BPV effect. Provided that a photocurrent flows parallel to the light polarization, the expected photocurrent  $J_{33}^*$  is written using an effective PV coefficient  $\beta_{33}^*$  as

$$J_{33}^* = \beta_{33}^* I_{\text{opt}}, \quad (6)$$

$$\begin{aligned} \beta_{33}^*(\theta, \phi) = & 2\beta_{15} \cos \theta \sin^2 \theta - \beta_{22} \sin^3 \theta \cos 3\phi \\ & + \beta_{31} \sin^2 \theta \cos \theta + \beta_{33} \cos^3 \theta, \end{aligned} \quad (7)$$

where  $\phi$  and  $\theta$  are the Euler angles, as defined in Fig. 4(a) [27].

In Fig. 4(a), we display the  $|\beta_{33}^*(\theta, \phi)|$  surface obtained from the BPV tensor elements using Eq. (7). In the cross section in the plane ( $\phi = 0^\circ, 0^\circ \leq \theta \leq 360^\circ$ ) [Fig. 4(b)], the maximum  $|\beta_{33}^*|$  ( $|\beta_{33}^*|_{\text{max}} = 1.1 \times 10^{-4} \text{ V}^{-1}$ ) is attained at  $\theta = 0^\circ$  and  $\phi = 0^\circ$ . The  $\beta_{\text{off}}^{\text{DW}}$  is more than three times as large as the  $|\beta_{33}^*|_{\text{max}}$ , despite all of the elements being averaged over the entire sample. This result demonstrates that the  $71^\circ$  DWs in our BFO film exhibit a giant PV effect, as previously proposed by Yang *et al.* [15]. We conclude that exploiting the DW-PV effect can achieve enhanced control of the PV properties beyond the BPV effect in the BFO system with  $71^\circ$  domain walls.

Here, we discuss the mechanism of the DW-PV effect. The DW-PV effect can be formulated by using  $\beta_{\text{off}}^{\text{DW}}$  and  $\beta_{\text{amp}}^{\text{DW}}$ . Considering the local polar feature and the ferroelastic distortion of the  $71^\circ$  DWs [20], we expect that the DW-PV effect arises from two contributions: an electrostatic potential step ( $\Delta\Phi_{\text{DW}}$ ) at the  $71^\circ$  DWs [28] and a local PV component

[21] in the  $71^\circ$  DW regions. Figure 5 shows the schematics of a spatial variation of  $\mathbf{P}_s$  in the  $x$ - $y$  plane across the  $71^\circ$  DW and its respective electronic band profile. Because the  $\mathbf{P}_s$  vector of the perovskite unit cells rotates [Fig. 5(c)], the DW region is forced to have a structural distortion, which is associated with a modulation of the  $y$  component of  $\mathbf{P}_s$  [28]. As a result,  $\nabla \cdot \mathbf{P}_s$  becomes nonzero and thus gives rise to  $\Delta\Phi_{\text{DW}}$  [8,29] [see Fig. 5(b)]. Under illumination with an energy greater than the band-gap energy, photoexcited electron-hole pairs generated in the DW regions are effectively separated by  $\Delta\Phi_{\text{DW}}$ , leading to a PV current flowing in the same direction as the net polarization. Because  $\Delta\Phi_{\text{DW}}$  does exist regardless of illumination and is not affected by  $\omega$ ,  $\Delta\Phi_{\text{DW}}$  contributes to  $\beta_{\text{off}}^{\text{DW}}$ .

Another factor, the local PV component of the DW-PV effect, stems from the intrinsic symmetry breaking in the  $71^\circ$  DW regions, which is quite different from that in the

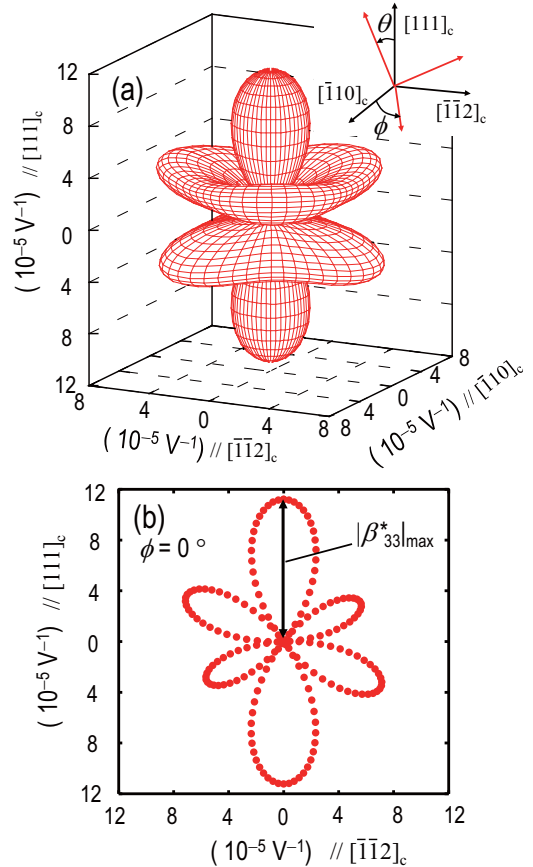


FIG. 4. (a) Effective PV coefficient surface  $|\beta_{33}^*(\theta, \phi)|$  obtained from the BPV tensor elements in the SD film. (b) Cross section of the  $|\beta_{33}^*|$  surface at  $\phi = 0^\circ$  in the  $\theta$  range from  $0^\circ$  to  $360^\circ$ . The coordinate system axes are along the pseudocubic axes.

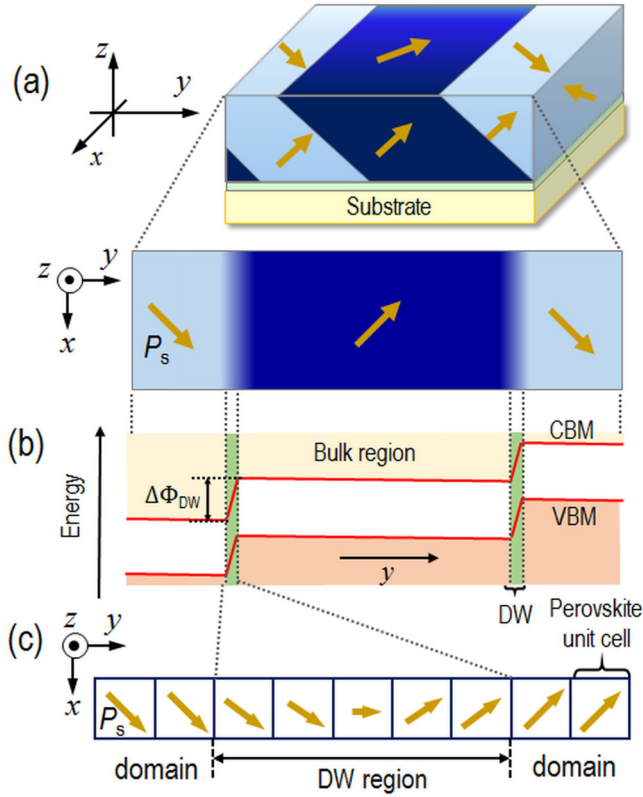


FIG. 5. Schematics of (a) domain structure, (b) electronic band profile, and (c) spatial variation of the  $\mathbf{P}_s$  vector in the  $y$  direction in the  $71^\circ$  DW region;  $P_s$  corresponds to the component of  $\mathbf{P}_s$  projected in the  $x$ - $y$  plane. VBM and CBM denote valence-band maximum and conduction-band minimum, respectively.

domains. Because the lattice in the  $71^\circ$  DW regions is subjected to a strong ferroelastic distortion caused by a spatial rotation of  $\mathbf{P}_s$  [see Fig. 5(c)], a PV response derived from the noncentrosymmetric nature is expected to emerge in the DW regions, as observed in  $90^\circ$  DWs in ferroelectric  $\text{BaTiO}_3$  crystals [21]. The spatial symmetry breaking in the DW

regions provides this local PV component, and the resultant photocurrent shows an  $\omega$  dependence. Thus, we consider that the local PV component in the DW region yields  $\beta_{\text{amp}}^{\text{DW}}$ . There is a possibility that the local PV component also provides an  $\omega$ -independent photocurrent and therefore has a certain contribution to  $\beta_{\text{off}}^{\text{DW}}$ , which will be investigated elsewhere.

Finally, we note that the PV properties of ferroelectrics in MD states must be investigated by taking into account both the BPV and DW-PV effects. The elements of these effects vary with temperature independently, and the BPV effect may overcome the DW-PV effect at low temperatures [16]. Moreover, specific atoms often accumulate preferentially at DWs because of large local strains [30], leading to a marked change in the DW-PV effect. The methodology adopted in our study provides reliable, unambiguous information about the physical origin of the PV effect in ferroelectrics with ferroelastic DWs.

#### IV. CONCLUSION

In this study, we have investigated the PV properties of the BFO films with the SD and MD structures. Our comprehensive analysis reveals that the BPV tensor determined for the SD film alone cannot explain the overall behavior and that the DW-PV effect considerably enhances the PV response. We demonstrate that the DW-PV effect plays a dominant role in the high photovoltages far exceeding the band gap observed for the MD film. Our methodology can clarify the contributions of these effects quantitatively and uncover a design strategy for enhancing ferroelectric photovoltaics.

#### ACKNOWLEDGMENTS

This research is supported by JSPS through Grant-in-Aid for JSPS Fellows (14J04693), partly by JSPS KAKENHI Grant No. 26249094, the Center for Integrated Nanotechnology at Tohoku University, and also the Nanotechnology Network Project of the Ministry of Education, Culture, Sports, Science, and Technology (MEXT) of Japan.

- [1] R. von Helmolt, J. Wecker, B. Holzapfel, L. Schultz, and K. Samwer, *Phys. Rev. Lett.* **71**, 2331 (1993).
- [2] G. R. Barsch and J. A. Krumhansl, *Phys. Rev. Lett.* **53**, 1069 (1984).
- [3] S.-E. Park and T. R. Shrout, *J. Appl. Phys.* **82**, 1804 (1997).
- [4] D. Damjanovic, *Rep. Prog. Phys.* **61**, 1267 (1998).
- [5] P. W. M. Blom, R. M. Wolf, J. F. M. Cillessen, and M. P. C. M. Krijn, *Phys. Rev. Lett.* **73**, 2107 (1994).
- [6] S.-W. Cheong and M. Mostovoy, *Nat. Mater.* **6**, 13 (2007).
- [7] I. V. Solovyev and Z. V. Pchelkina, *Phys. Rev. B* **82**, 094425 (2010).
- [8] B. Meyer and D. Vanderbilt, *Phys. Rev. B* **65**, 104111 (2002).
- [9] G. Catalan, J. Seidel, R. Ramesh, and J. F. Scott, *Rev. Mod. Phys.* **84**, 119 (2012).
- [10] T. Sluka, A. K. Tagantsev, D. Damjanovic, M. Gureev, and N. Setter, *Nat. Commun.* **3**, 748 (2012).
- [11] S. Wada, S. Suzuki, T. Noma, T. Suzuki, M. Osada, M. Kakihana, S.-E. Park, L. E. Cross, and T. R. Shrout, *Jpn. J. Appl. Phys.* **38**, 5505 (1999).
- [12] J. R. Teague, R. Gerson, and W. J. James, *Solid State Commun.* **8**, 1073 (1970).
- [13] J. Wang, J. B. Neaton, H. Zheng, V. Nagarajan, S. B. Ogale, B. Liu, D. Viehland, V. Vaithyanathan, D. G. Schlom, U. V. Waghmare, N. A. Spaldin, K. M. Rabe, M. Wuttig, and R. Ramesh, *Science* **299**, 1719 (2003).
- [14] F. Johann, A. Morelli, and I. Vrejoiu, *Phys. Status Solidi B* **249**, 2278 (2012).
- [15] S. Y. Yang, J. Seidel, S. J. Byrnes, P. Shafer, C.-H. Yang, M. D. Rossell, P. Yu, Y.-H. Chu, J. F. Scott, J. W. Ager, L. W. Martin, and R. Ramesh, *Nat. Nanotechnol.* **5**, 143 (2010).
- [16] A. Bhatnagar, A. R. Chaudhuri, Y. H. Kim, D. Hesse, and M. Alexe, *Nat. Commun.* **4**, 2835 (2013).
- [17] S. M. Young and A. M. Rappe, *Phys. Rev. Lett.* **109**, 116601 (2012).

- [18] A. M. Glass, *Appl. Phys. Lett.* **25**, 233 (1974).
- [19] S. M. Young, F. Zheng, and A. M. Rappe, *Phys. Rev. Lett.* **109**, 236601 (2012).
- [20] J. Seidel, L. W. Martin, Q. He, Q. Zhan, Y.-H. Chu, A. Rother, M. E. Hawkrige, P. Maksymovych, P. Yu, M. Gajek, N. Balke, S. V. Kalinin, S. Gemming, F. Wang, G. Catalan, J. F. Scott, N. A. Spaldin, J. Orenstein, and R. Ramesh, *Nat. Mater.* **8**, 229 (2009).
- [21] R. Inoue, S. Ishikawa, R. Imura, Y. Kitanaka, T. Oguchi, Y. Noguchi, and M. Miyayama, *Sci. Rep.* **5**, 14741 (2015).
- [22] H. W. Jang, D. Ortiz, S.-H. Baek, C. M. Folkman, R. R. Das, P. Shafer, Y. Chen, C. T. Nelson, X. Pan, R. Ramesh, and C.-B. Eom, *Adv. Mater.* **21**, 817 (2009).
- [23] S. Nakashima, Y. Takada, S. Seto, H. Fujisawa, O. Sakata, Y. Katsuya, M. Kobune, and M. Shimizu, *Jpn. J. Appl. Phys.* **52**, 09KB03 (2013).
- [24] W. Ji, K. Yao, and Y. C. Liang, *Phys. Rev. B* **84**, 094115 (2011).
- [25] See Supplemental Material at <http://link.aps.org/supplemental/10.1103/PhysRevB.94.214111> for detailed calculation methods for the analytic equations of the photocurrents in both the single-domain and the multidomain thin films.
- [26] H. G. Festl, P. Hertel, E. Krätzig, and R. von Baltz, *Phys. Status Solidi B* **113**, 157 (1982).
- [27] D. Damjanovic, M. Budimir, M. Davis, and N. Setter, *J. Mater. Sci.* **41**, 65 (2006).
- [28] A. Lubk, S. Gemming, and N. A. Spaldin, *Phys. Rev. B* **80**, 104110 (2009).
- [29] Y. Kitanaka, Y. Noguchi, and M. Miyayama, *Phys. Rev. B* **81**, 094114 (2010).
- [30] S. Farokhipoor, C. Magén, S. Venkatesan, J. Íñiguez, C. J. M. Daumont, D. Rubi, E. Snoeck, M. Mostovoy, C. de Graaf, A. Müller, M. Döblinger, C. Scheu, and B. Noheda, *Nature (London)* **515**, 379 (2014).